# SEA SPECTRA AS DETERMINED FROM LOW-ALTITUDE SLAR IMAGES

Konstantin Voliak
General Physics Institute of USSR Ac. Sci.
38 Vavilov st., 117942 Moscow, USSR, Commission VII

ABSTRACT. The analytic composite theory for the surface of Gaussian slope statistics has revealed that backscattering of vertically (V) polarized microwaves from the sea at large angles of incidence might have an azimuthal characteristic, which corresponds to the angular dependence of the small-scale Bragg spectrum, with an accuracy to within the slope variance of long waves. For horizontally (H) polarized radiowaves, the model relates the image speckles to the statistics of spikes in a random surface-wave field. Fourier analysis and photometering of radioimages taken over various seas have allowed us to estimate the spectra of large- and small- scale sea surface waves as well as to study other phenomena imprinted on surface waves.

1. INTRODUCTION. Imaging radars yield principally novel data on the physical state of the sea. The aim of this paper is to develop simple models for image formation by an airborne real-aperture side-looking radar (SLAR) at different polarizations as well as to elaborate experimental methods and data processing techniques to effectively extract sea parameters, particularly wave spectra, from radioimages.

2. THEORY OF MICROWAVE SCATTERING FROM THE SEA SURFACE. Microwave backscatter from highly conducting surfaces, including the sea, depends strictly on polarization. At fairly large angles of incidence, $\theta$ , the H-polarized backscattered Bragg power is notably weaker than the V- polarized one. Generally the V-polarized power (Fig. 1a) shows up in a scattered field of the first order, which is rather smoothly modulated by sea surface features. On the other hand, an H-polarized backscatter (Fig.1b) produces an image formed by randomly spaced bright spots, or by the so-called speckles, whereas the Bragg return is virtually at the noise level. A similar temporal behavior of polarized scattered fields was first established by Long. [1].
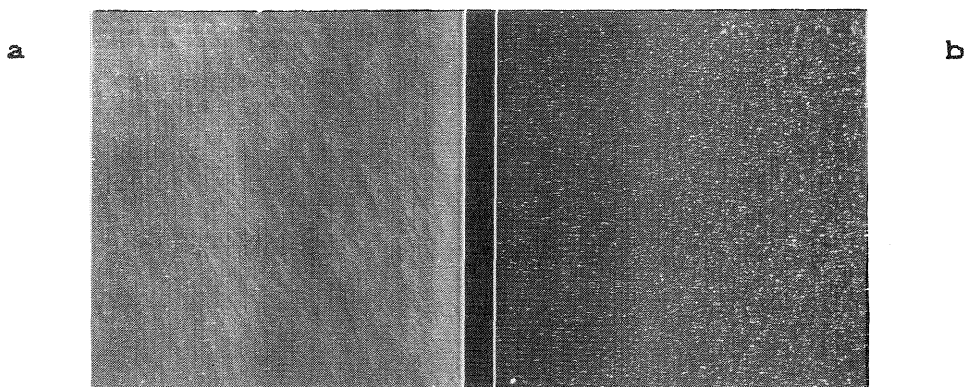


Fig.1. Sea radiomages of a 10x10km area as taken at a wavelength $\lambda \simeq 2.25$ cm : V-polarization (a) and H-polarization (b) in mirror symmetry; the figure axis is the aircraft heading line

The composite theory allows us to decode V-polarized SLAR images of the sea. Assuming that the conventional specular component and the second-order scatter, i.e. depolarization, are negligible at $\theta > 30°$, we can write a local cross-section of V-backscattering [2]:

$$\sigma^V(\theta, \alpha, \beta) = k_o^4 \cot^4\theta_i |G|^2 W(2k_o \sin\theta', 2k_o \cos\theta' \sin\beta), \qquad (1).$$

where $k_o = 2\pi\lambda^{-1}$, $\cos\theta_i = \cos\theta' \cos\beta$, $\theta' = \theta + \alpha$, $\alpha$ and $\beta$ are the angles between the smoothed surface and the horizon in the plane of incidence and in the plane normal to the latter, $\varepsilon$ is the dielectric constant, $W(K_x, K_y)$ is the roughness spectrum, the x-axis lies in the plane of incidence,

$$G = [\varepsilon(1 + \sin^2\theta_i) - \sin^2\theta_i]T_1 \sin^2\theta' \cos^2\beta + T_2 \sin^2\beta, \qquad (2)$$

$$T_1 = (\varepsilon - 1)(\varepsilon\cos\theta_i + \sqrt{\varepsilon - \sin^2\theta_i})^{-2}, T_2 = (\varepsilon - 1)(\cos\theta_i + \sqrt{\varepsilon - \sin^2\theta})^{-2}.$$

The average cross-section, $\sigma_o^V$, is determined by an integral over all the slopes within an irradiated area:

$$\sigma_o^V(\theta) = \iint \sigma(\theta, \alpha, \beta) p(\tan\alpha, \tan\beta) d(\tan\alpha) d(\tan\beta), \qquad (3)$$

where, neglecting the shadowing factor,

$$p(\tan\alpha, \tan\beta) = p_o(\tan\alpha', \tan\beta') \cos\theta_i / \cos\theta, \qquad (4)$$

$p_o(\tan\alpha', \tan\beta')$ is the anisotropic probability density of sea slopes along its principal axes, the coefficient $\cos\theta_i / \cos\theta$ is related to the 'area defect' in the slope distribution, observed at an angle of incidence $\theta$ [3]. The averaged value of (3) is conventionally computed for an isotropic normal distribution without any areal correction and for a certain (usually isotropic) spectral model. However, $\sigma_o^V$ can be also evaluated analytically avoiding numerical computations.

2.1 Radar Gross-Section Evaluation. The actual long-wave slopes are small, $|\alpha|$, $|b| = O(\mu) \ll 1$, and their distribution is approximately Gaussian [4]. Within a fairly good accuracy $O(\mu^2)$ for slightly rough seas, i.e. neglecting the slope skewness, we can replace the tangents of small angles in (3), (4) by their arguments. Further, assuming $|\varepsilon| \approx 100$ for cm and dm microwaves, the calculation of $\sigma^V$ reduces to a series expansion of $|G|^2 \cot^4\theta$ and $W(2k_o \sin\theta', 2k_o \beta^o \cos\theta')$ in $\mu$ and $|\varepsilon|^{-1/2}$, followed by their product averaging over slope distribution (4). Here, we can restrict ourselves to the terms $O(|\varepsilon|^{-1/2}, \mu^2)$. The result, accurate to a few per cent, is

$$\sigma_o^V(\theta, \varphi) = Bk_o^4(1 + \sin^2\theta)^2(2k_o \sin\theta)^{-S}|1 + (\sqrt{\varepsilon} \cos\theta)^{-1}|^4 f(\varphi) M, \qquad (5)$$

where $\varphi$ is the azimuthal angle along the principal axes, the typical roughness spectrum is given by the power-law [5]

$$W(K, \varphi) = BK^{-S} f(\varphi), \qquad (6)$$

the modulation is expressed by

$$M = M(\bar\alpha, \alpha_o, \bar\beta, \beta_o) = 1 + m_1\bar\alpha + m_2\bar\beta + m_{11}\alpha_o^2 + m_{12}\beta_o\alpha_o + m_{22}\beta_o^2 + O(|\varepsilon|^{-1}, \mu^3),$$

$\bar{\alpha}$ and $\bar{\beta}$ are the average slopes, the tilt the variance $(m_1, m_2,$ and $m_{11}, m_{12}, m_{22})$ modulation transfer functions (m.t.f.'s) depend evidently on $\theta$, $|\varepsilon|^{-1/2}$, s, and $f(\varphi)$ .

2.2 Tilt and Variance Modulation. The m.t.f.'s behave quite differently with respect to $\theta$. For instance, at a saturated spectrum (6) of the actual azimuthal factor [3], assuming s=4, $|f'/f| \leqslant 0.5$, $|f''/f| \leqslant 1$, the functions $m(\theta)$ are similar to those in Fig.2. They are calculated for $\lambda = 2.5$ cm, i.e. for (cf.[6]) $\varepsilon = 50-35i$.
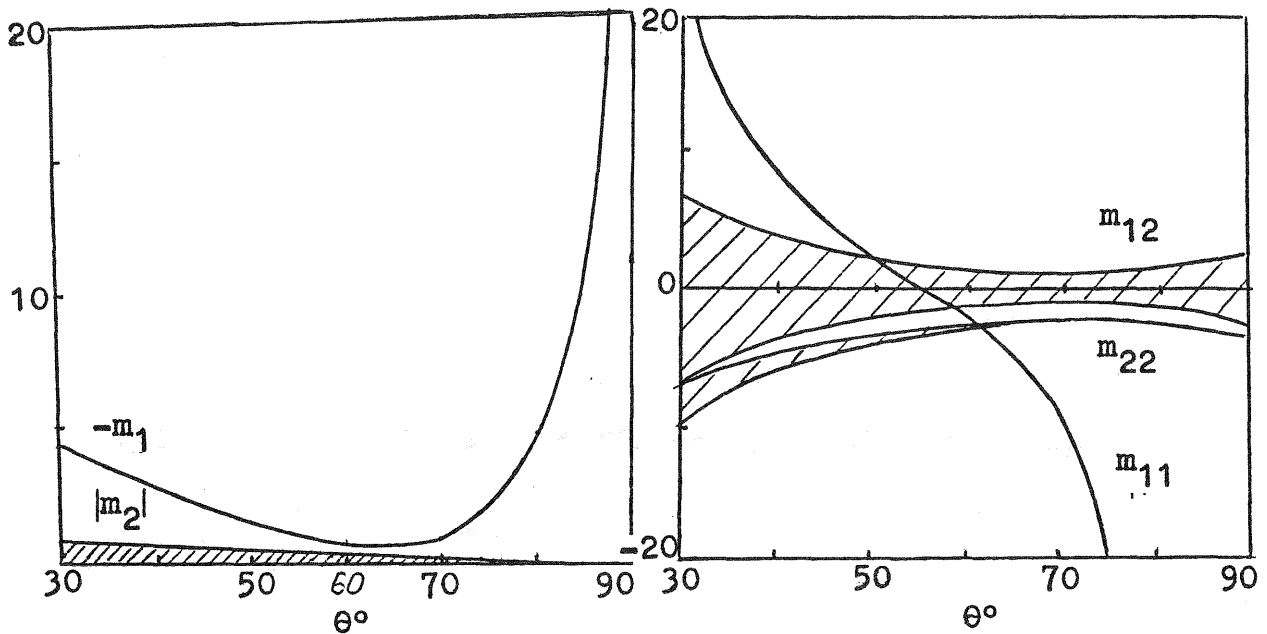


Fig.2. M.t.f's versus $\theta$ for $\lambda = 2.5$ cm,
$|f'/f| \leqslant 0.5$, $|f''/f| \leqslant 1$

When $\theta \leqslant 70°$ the power scattered from an anisotropic sea is modulated in a complex way by all the slope components. In this case, the backscatter from isotropic waves [2],[7] is slightly sensitive to slopes owing to the small m.t.f's , when $\theta > 71°$, however, $|m_1| \gg |m_2|$, $|m_{11}| \gg |m_{22}|$, $|m_{12}|$ , and the modulation arises primarily from the slopes of long waves oriented in the plane of incidence. At grazing angles, $|m_1|$, $|m_{11}|$ are proportional to $\tan \theta$ , $\tan^2\theta$ , respectively. Hence , the modulation by such slopes should predominate over other [7] scatter modulation types, which are somewhat limited. The number of s has a very slight bearing on the m.t.f's and, as it changes from 3.5 to 4.5, the considered angles are shifted only by 1.5°. These m.t.f's occur over a wavelength range up to $\lambda = 1$m, while the angles shift slightly towards $\theta = 90°$.

2.3. Radar Measurement of Bragg Resonant Wave Spectra. Another form of (6) yields

$$\sigma_o^v(\theta,\varphi) = (1+\sin^2\theta)^2 |1+(\sqrt{\varepsilon}\cos\theta)^{-1}|^4 W(k_o\sin\theta,\varphi)[1+\alpha(\mu,|\varepsilon|^{-1})]. (7)$$

Thus, by measuring the backscattered power at various azimuths and angles of incidence and by averaging it over the longest sea wavelength, we can define, accurate to an order of long-wave

slope variance, i.e. to a few per cent, the directional spectrum $W(K,\varphi)$ of short resonant waves of $\lambda = \pi(k \sin\theta)^{-1}$. For isotropic long waves, (7) agrees with the numerical findings [2]. It is also clear that (7) implies an accordance between the azimuthal anisotropy of $\sigma^v(\varphi)$ and the angular spreading $f(\varphi)$ (6). For large averaging scales, all the conclusions drawn are also valid, sometimes at the expense of accuracy, for any kind of scatter modulation [7]. For directional spectrum measurements, SLARs and synthetic aperture radars (SARs) are most suitable. If their antenna vertical aperture admits angles $30° \leqslant \theta \leqslant 90°$, the measured spectral range can be as large as $\Delta K = 2K(\theta = 30°)$. The high spatial resolution of SARs and SLARs permits, in principle, a more accurate spectral measurement than is achievable with conventional scatterometers. The azimuth can be varied by changing the aircraft heading.

2.4. Long-Wave Spectra from an Image Fourier Analysis. The problem of how an image Fourier-transform can conform to the actual sea is still disputable. It can be resolved, on the basis of the foregoing examination, for angles of $70-80°$ and moderately developed seas. A SLAR operates as a low-pass filter with a cut-off at $K_L = 2\pi L^{-1}$, L being resolution. Then, in the first approximation, the images recorded at $\varphi = $ const correspond for $\lambda > L$ to a spatial pattern of the smoothed slope $\alpha_\varphi = \alpha$ in the azimuthal plane. A Fourier transform of the image yields distribution of $\alpha_\varphi$ in wave numbers and directions.

Following [8], we examine the transformation of a coherent plane light wave passing through a radioimage modulated in amplitude as

$$T(\bar{R}) = T_0 [1 + \dot{m}_{10} \alpha_\varphi (\bar{R})], \qquad (8)$$

where $\bar{R} = (X,Y)$ is the coordinate in the image; $T_0$ is its average transparency; $m_{10}$ is the mean value of $m (\cos^4 h/Y)$; h is the SLAR altitude; $Y^4$ stands for the range. The light intensity in an off-axis region in the focal plane of a converging lens is proportional to

$$I(\bar{K}) = \left| \iint \alpha_\varphi (\bar{R}) \exp(-i\bar{K}\bar{R}) d\bar{R} \right|^2 , \qquad (9)$$

where $\bar{K}$ is the radius vector in the plane of transform. Measuring intensity (9), we determine the directional spectrum of long-wave slopes $\alpha_\varphi$.

3. MODEL OF H-RADIOIMAGE FORMATION. At oblique angles of incidence, the Bragg H-scatter may be a few dozens of decibels lower than that of specular reflection and the so called 'wedge' [10] scatter. The two mechanisms occur only at the surface of breaking or nearbreaking waves. This point is corroborated by numerous experiments, in which a noticeable H-backscattering appears simultaneously with the onset of white capping. A spike of the reflection, even averaged over radar resolution may prove an order of magnitude more intense than the Bragg background and, hence, may produce a saturated density of recording films. Thus. each bright spot should be referred to a site at the sea that has undergone breaking during irradiation. To develop a simple model of the phenomenon, we assume that

there exists a certain limiting amplitude of waves. If the amplitude is exceeded, waves are no longer stable and start to break [9]. Then, the speckle statistics in images reduces, in general, to the statistics of overthrowings of a two-dimensional random function above a specified height level.

3.1. Statistics of a Random Sea Surface. To simplify the solution to the problem, we consider the Gaussian field of sea waves because their actual statistics differs just slightly from the normal case [4]. Most important for us is the mean number $N_a$ of overthrowings of the random function $\zeta(x,y)$ above some appropriate level $\zeta = a$ per unit area. If the level a is fairly high, the number of overthrowings for an anisotropic random Gaussian field is determined by [11]

$$N_a = (m_{20} m_{02} - m_{11}^2)^{1/2} (2\pi m_{00})^{-3/2} a \, \exp(-a^2/2m_{00}) \, , \qquad (10)$$

where $m_{ij} = \iint\limits_{-\infty}^{\infty} W(K_x, K_y) K_x^i K_y^j dK_x dK_y$ stands for spectral momenta.

Take simple power-law spectrum (6) in the range $K_o \leqslant K \leqslant K_4$ as a saturated sea model, where $K_o$ corresponds to the high-energy component, $K_4$ is the high-frequency cut-off. This yields the momenta and (10) changes over to

$$N_a = (\pi f_{00})^{-\frac{3}{2}} B^{-\frac{1}{2}} (f_{02} f_{20} - f_{11}^2)^{\frac{1}{2}} (\ln \frac{K_4}{K_o}) K_o^3 a \, \exp(-\frac{a^2 K_o^2}{B f_{00}}) , \qquad (11)$$

where $f_{ij} = \int\limits_{0}^{2\pi} f(\varphi) \cos \varphi^i \sin \varphi^j d\varphi$ .

Hence, we see that the speckle density depends strongly on the typical width $f_{00}$ of an azimuthal spreading. Another important feature is the exponential dependence of $N_a$ on the square of breaking wave steepness $(aK_o)^2$. It is noteworthy that measurement of speckle density in images is a very special procedure. A more common practice is photometering of an image density. A description of this operation shows that, at Gaussian seas, the mean signal obeys largely the same rules as does the number of spikes.

3.2. Current-Induced Variations in the Spike Statistics. If a surface wave runs to an inhomogeneous surface current $\overline{U} = \overline{U}(x,y)$, the former and the latter undergo an energy exchange. Waves over an opposite-directed current are supplied by the energy from it, while, in the case of a divergent current, the reverse effect occurs. To analyze the spike statistics of the sea on currents which are due, for example, to internal waves, we use the conservation law of kinematic wave density

$$\nabla(\sigma + \overline{KU}) = \sigma_o , \qquad (12)$$

where $\sigma = (gK)^{1/2}$ is the wave frequency at $\overline{KU} = KU\cos\varphi = 0$. Using (12), we obtain variations in the wave number

$$K' = 4K[1 + (1 + 4U\sqrt{K/g} \, \cos\varphi)^{\frac{1}{2}}]^{-2} = K(1 - 2U\sqrt{K/g} \, \cos\varphi) + (U\sqrt{K/g}) \, . (13)$$

For saturated spectra on the current, the high-energy and the

cut-off components shift as $K_o \to K_o'$ and $K_1 \to K_1'$, respectively. Substituting (13) into (10), we derive variations in $N_a$ on the current U

$$\Delta N_a / N_a \propto -U\cos\varphi \ [1 + \propto a^2 K_o^2)] \ . \tag{14}$$

Thus, the speckle density in H -radioimages increases on currents moving against the wind and decreases in the opposite case. In addition, we evaluate the nonlinear effects in the speckle statistics and estimate essential corrections $\propto aK_o)$ to the speckle density due to the second-order nonresonant nonlinearity of gravity waves.

4. EXPERIMENTS. 4.1. Experimental Procedures. Circular flights, which are conventional in azimuthal measurements [3], have been undertaken. A SLAR operated at $\lambda \approx 2.25$ cm was installed aboard the Antonov-24 aircraft of the 'Aeroflot' Co. Due to the high spatial resolution of the instrument we have taken azimuthal scattering characteristics in detail. The flights were performed in the coastal areas of the Pacific near Kamchatka and of the Barents Sea. near Kola Peninsula as well as in the Black Sea. The other flights were various 'boxes' and 'stars', similar to that of Fig. 3.
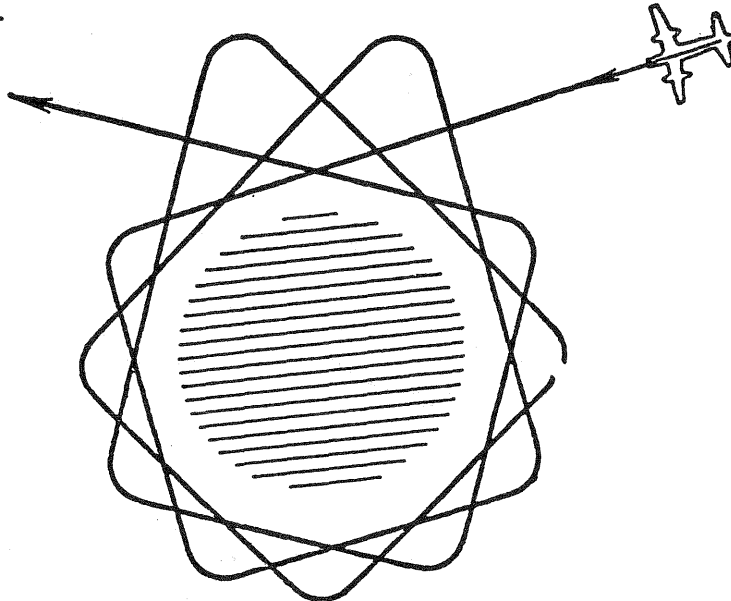


Fig. 3. Aircraft 12-tack flight of the 'rotating box'-type

4.2. Azimuthal Measurements. With stable SLAR parameters, an average image density is proportional to the scattering cross section. Fig. 4 shows $\sigma$ for V-polarized (crosses) and H-polarized (dots) scatter versus azimuth $\varphi$ . The scattering was averaged over an area of $500 \times 250$ $m^2$ $(3 \times 1.5^{\circ})$ at $\theta = 57^{\circ}$, and then normalized to its maximum. The ratios of the circle diameters presented of Figs.4 a,b to that in Fig.4 c are $0.1 : 1$ and $0.72: 1$, respectively. The weather conditions shown in the caption were reported by a ship drifting 20 km away from the center of the experiment area.

The azimuthal characteristics have conventionally an axis of symmetry coinciding with the wind direction, so Fig.4a suggests,

for instance, the direction of a calm breeze. Figs. 4b and c differ very strongly in spite of close wind velocities. Thus unlike [3], this velocity is not a single parameter determining the backscatter. Its nature is quite different for different polarizations. Evidently, at V-polarization only Fig. 4c corresponds within a fairly good accuracy to the actual spreading f($\varphi$) for capillary-gravity waves of $\lambda$=1.3cm. According to the theory, this accuracy is provided by a deep azimuthal dependence of $\sigma$ and by virtually symmetric scatter related to the wind direction. The other two V-characteristics reproduce f($\varphi$), involving some distortions due to the skewness of long-wave slopes. While H-scattering is, in practice, isotropic under the calm (Fig. 4a), it is highly anisotropic even at moderate winds (Figs. 4b , c). Processing the azimuthal characteristics for the H-backscatter in the sector $\theta = 45-60°$ yields the second spectral momenta and estimates nonlinear skewness and curtosis of long-wave slopes. It is remarkable that the estimates are in a very good accordance with [12], while those made according to [4] under our experimental conditions, are considerably higher.
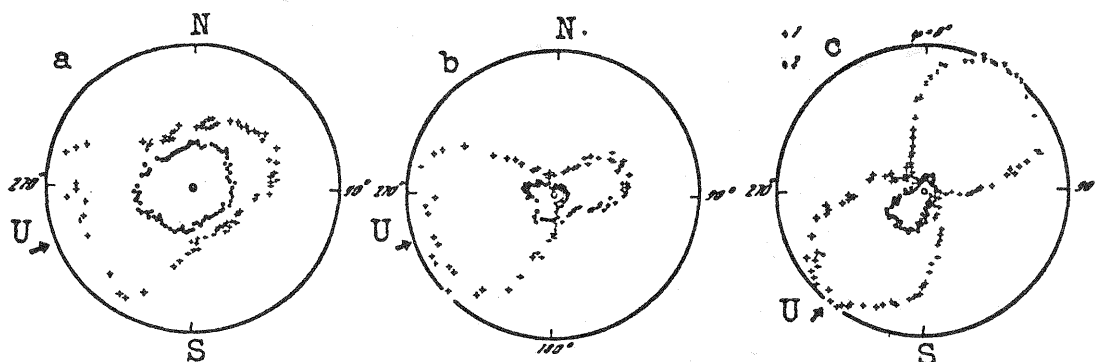


Fig. 4. Azimuthal characteristics $\sigma(\varphi)$ at $\theta = 57°$: crosses – V-polarization, dots – H-polarization ; (a) calm, U = 0, (b) steady wind, U = 6 ms$^{-1}$, (c) gusty wind, U= 6 – 8 ms$^{-1}$

4.3. Fourier Analysis of Sea Radioimages. Two-dimensional Fourier transform of radioimages is observed in the focal plane of a converging lens in a coherent optical system [8]. V-images, taken over each of the 12 tacks of the flight and shown in Fig.3, were processed in the analyzer. A series of optical spectra is presented in Fig.5, where each spectrum is placed at the azimuth of an original image. In the center, there is a spectrum of reference grating with $\lambda$ = 50m.

A feature of importance to us is the disappearance of waves at azimuths orthogonal to the wind, namely,at $\varphi$ = 150, 180, 330, and 0°. Conversely, in directions almost collinear to the wind, the waves are clearly pronounced. This confirms the theory

asserting the predominant modulation of V- backscatter by long-
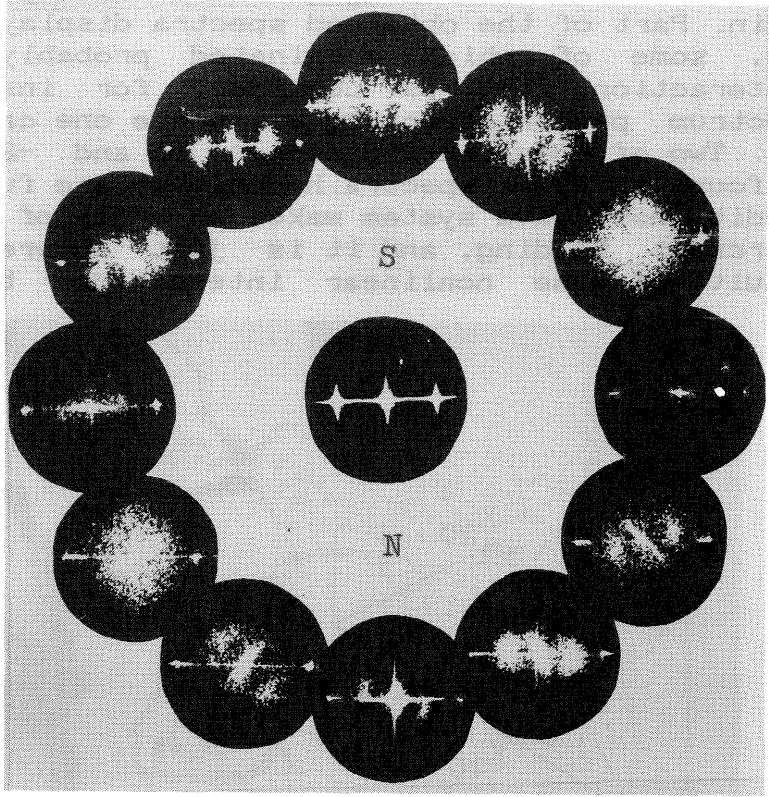wave slopes.



Fig.5. Optical spectra of the 12 SLAR 'rotating box' tacks

4.4. Spectra of Short-Wave Resonant Roughnesses. The radar
cross-section for each of the 12 azimuths was determined by
measuring the image density versus slant range. Using a
transform inverse to (7), the spectral density $W(2k\ \sin\theta)$ was
computed. Fig.6. shows 12 of such spectra cut-off at $\theta < 70°$
to avoid strong modulations and covering the total azimuthal
circle. At $42 \leqslant \theta \leqslant 70°$ all the spectra decline with increasing
$\theta$ to obey the universal power-law $W(K) \propto K^{-5.1\pm0.2}$. Note that
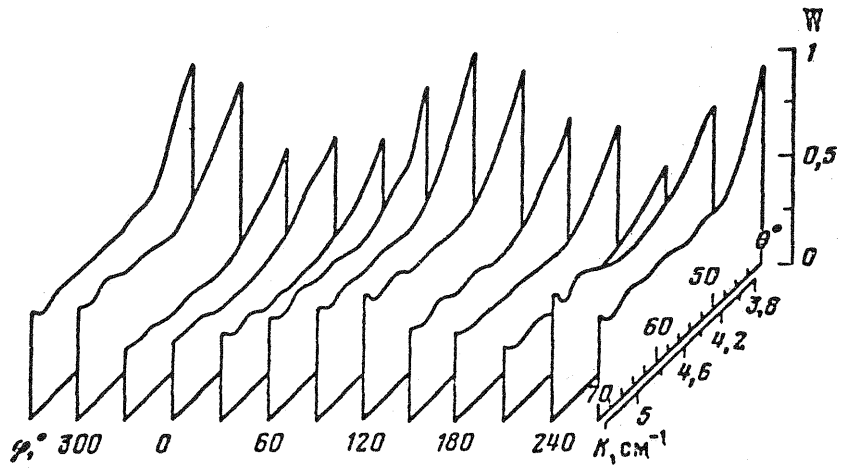these angles cover the wavelengths $1.2 \leqslant \lambda \leqslant 1.7$ cm.



Fig.6. Resonant-wave spectrum $W(K)$ versus azimuth $\varphi$
as determined from the 12 SLAR tacks

4.5. Nonlinear Wave Interaction as Observed by an Imaging Radar.
The typical Pacific radioimages were analyzed in a
spectral domain. Part of the obtained spectra displayed several
wave systems, some of which originated probably from the
nonlinear interaction. Let us consider, for instance, the
smoothed spectrum presented in Fig. 8., where one can see three
wave systems. Two of them, making angles 55 and $-25°$ with the
horizon, are found in other spectra. Hence, they are fundamentals.
The third (additional) wave system makes an angle of around $30°$
with the aircraft heading, and it is just interesting as a
probable result of the nonlinear interaction between the
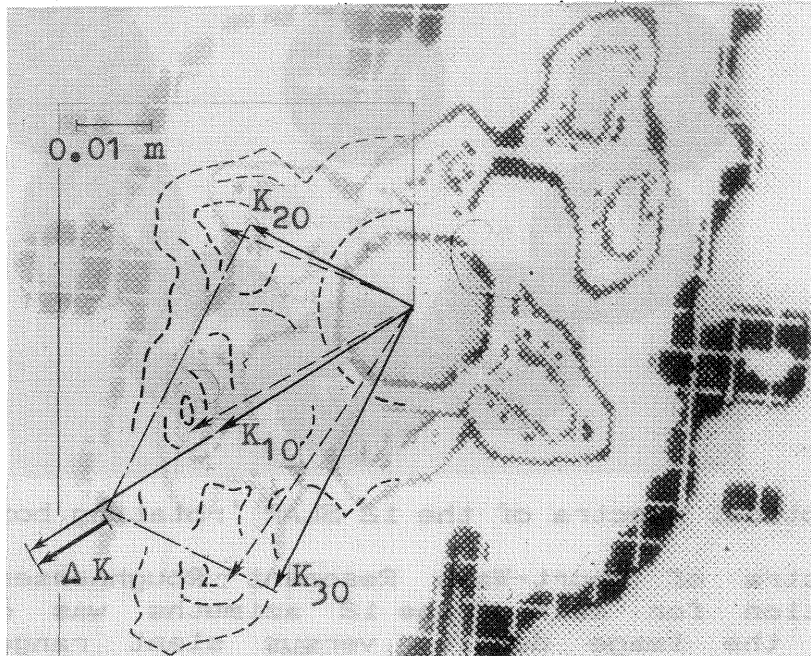fundamentals.



Fig. 7. Smoothed radioimage spectrum and corrected
wave vectors near the spatial resonance

To verify the hypothesis, Fig. 8. plots the spatial resonance for
the vectors of the additional (central) wave $K_4$ and of the
fundamental (side) waves $K_2$, $K_3$. This plot is superimposed on
the equal spectral density lines after corrections, to
account for the relative motion of the platform referred to the
sea scatterers. It results in the fact that the frequency
resonance $K_{20}^{1/2} + K_{30}^{1/2} = 2K_{10}^{1/2}$ is fulfilled within a very good
accuracy, while the considerable phase detuning
$\Delta K = 2\bar{K}_{10} - \bar{K}_{20} - \bar{K}_{30}$ is measured from Fig. 10.

It follows from theory that such nonsynchronous waves interact
quasistationarily. Thus, the central wave component is expected
to have some spatial beats. To check this claim, the spectrum of
Fig. 8 was multiplied by a binary filter, which is totally
transmitting over a sector $20°$ oriented along $\bar{K}_{10}$ and
nontransparent in other directions. The product was Fourier-
transformed. The density of the reconstructed image is presented
in Fig. 9. Here one can see the spatial beats of a period of
450-700m marked with broken lines. The theoretical spatial period
was estimated to be about 500 m, which is close to the beats in
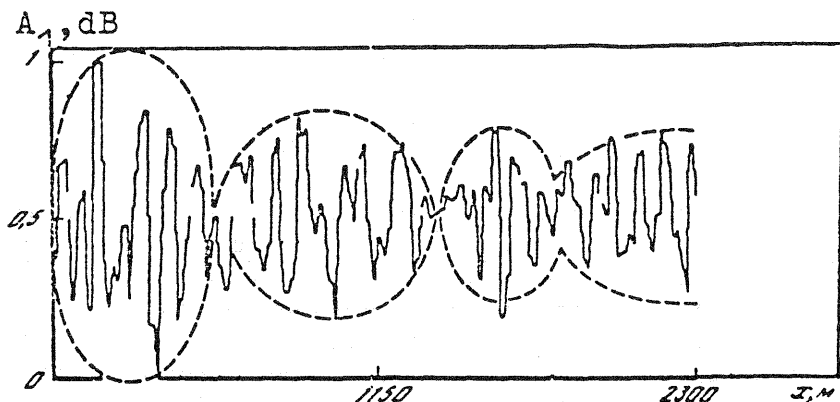the filtered-out image.

A$_1$,dB

Fig.8. Spatial beats of the central-wave amplitude as a result of the image processing

5. CONCLUSIONS. (i) The modulation of the sea radioimages of V-polarization, taken at oblique angles, is due to the long-wave slopes in the plane of antenna look. (ii) The speckles of H-polarized sea radioimages are explained by the statistics of specular reflections and wedge scatter from steep waves. The speckle structure depends strongly on the directional spectrum and nonlinearity of the sea as well as on the inhomogeneous surface currents. (iii) The developed models provide imaging radar methods to be used for experimental measurement of sea spectra of different scales and for observation of the effects of various atmospheric and oceanic processes.

6. REFERENCES

1. Long M.W. On a two-scatterer theory of sea echo.
   IEEE Trans. Antennas Propagat. AP-22, 667-672, 1974.
2. Valenzuela G.R., Laing M.B. and Daley L.C. Ocean spectra for the high-frequency waves as determined from airborne radar measurements. J. Marine Res. 29, 69-84, 1971.
3. Moore R.K. and Fung A.K. Radar determination of winds at sea. Proc. IEEE 67, 1504-1521, 1979.
4. Cox C. and Munk W. Measurement of roughness of the sea surface from photographs of the sun's glitter. J. Opt. Soc. Amer., 11, 838-850, 1954.
5. Phillips O.M. The Dynamics of the Upper Ocean. Camb. Univ. Press, Lond., 1977.
6. Saxton J.A. and Lane J.A. Electrical properties of sea water. Wireless Eng. 29, 269-275, 1952.
7. Alpers W.R., Ross D.B. and Rufenach C.L. On the detectability of ocean surface waves by real and synthetic aperture radar. J. Geophys.Res. C86, 6481-6498, 1981.
8. Goodman J.W. Introduction to Fourier Optics. McGraw-Hill, N.Y., 1968.
9. Longuet-Higgins M.S., On wave breaking and the equilibrium spectrum of the wind-generated waves. Proc. Roy. Soc. Lond. A310, 151-159, 1969.
10. Lyzenga D.R., Maffett A.L.and Shuchman R.A. The contribution of wedge scattering to the radar cross section of the ocean surface. IEEE Trans. Geosci. Remote Sens. GE-21, 502-505, 1983.
11. Nosko V.P. Determination of the number of random field overthrowings above a fixed level. Teorija Verojatnostej i Jejo Primenenija 24, 592-596, 1979.
12. Longuet-Higgins M.S. The effect of non-linearities one statistical distributions in the theory of sea waves. J.Fluid Mech. 17, 459-480, 1963.